Schweizerischer Erdbebendienst
Service Sismologique Suisse
Servizio Sismico Svizzero
Swiss Seismological Service

ETH zürich

SITE CHARACTERIZATION REPORT
SCRM: Crans-Montana (VS), Hôpital

Paolo Bergamo, Dario Chieppa, Donat Fäh

Last modification: 14.05.2022

Schweizerischer Erdbebendienst (SED)
Service Sismologique Suisse
Servizio Sismologico Svizzero
Servizi da Terratrembels Svizzer

ETH Zurich
Sonnegstrasse 5
8092 Zuerich
Schweiz
paolo.bergamo@sed.ethz.ch

Contents

Summary

The new SSMNet station SCRM was installed (11.7.2019) in the territory of the municipality of Crans-Montana (VS), at the Clinique de Réhabilitation des Hôpitaux Universitaires de Génève (Impasse Clairmont 2). The geographical setting is the north-western slope of the mid Swiss Rhône valley, whose surficial geology is characterized by scree deposits intertwined with moraines (till); in particular, station SCRM is located on top of a thin moraine deposit, overlying metasedimentary schists. Active seismic measurements, as well as a single-station noise recording survey, were performed to characterize the subsurface structure beneath the station.

The fundamental frequency (f_0) of the site, identified on the horizontal-to-vertical spectral ratio of noise recordings, is 14 Hz; this value ius associated with the sharp velocity contrast, estimated at 3.5 m depth, between the surficial soil ($V_S \approx 200$ m/s) and the moraine underneath ($V_S \approx 1200$ m/s). This moraine layer should extend down to a depth of ~7 m. Between 7 and 14 m depth the S-wave velocity increments further to ~1600 m/s. This value could be attributed to a compact moraine rich in gravel, or to a schists formation. Between 14 and 40 m depth, the estimated S-wave velocity ranges between 1000 and 1250 m/s; this layer is probably constituted by weathered clayey/chalky schists, responsible for the mass movement affecting the area. Further below, at around 40 m depth, the V_S increases to ~2000 m/s, indicative of a stiffer rock material.

The estimated V_{S30} value is 728 m/s, which classifies the site as B type according to both SIA261 (SIA, 2020) and Eurocode 8 (CEN, 2004) standards. The engineering bedrock (H800, depth to shallowest layer with $V_S > 800$ m/s) is at 3.5 m depth.

1. Introduction.

In the framework of the second phase of the SSMNet (Swiss Strong Motion Network) renewal project, a new station, labelled as SCRM, was installed and started operating on 11.07.2019 in the territory of the municipality of Crans-Montana (VS), at the clinique Génevoise (hamlet of La Comba, Figure 1 and Figure 2, top panel). The host site is located on the north-western flank of the mid Swiss Rhône valley, at an altitude of 1473 meters above sea level. An active seismic survey and a single-station ambient noise measurement were carried out on 20.10.2021 to ensure the seismic characterization of the site.

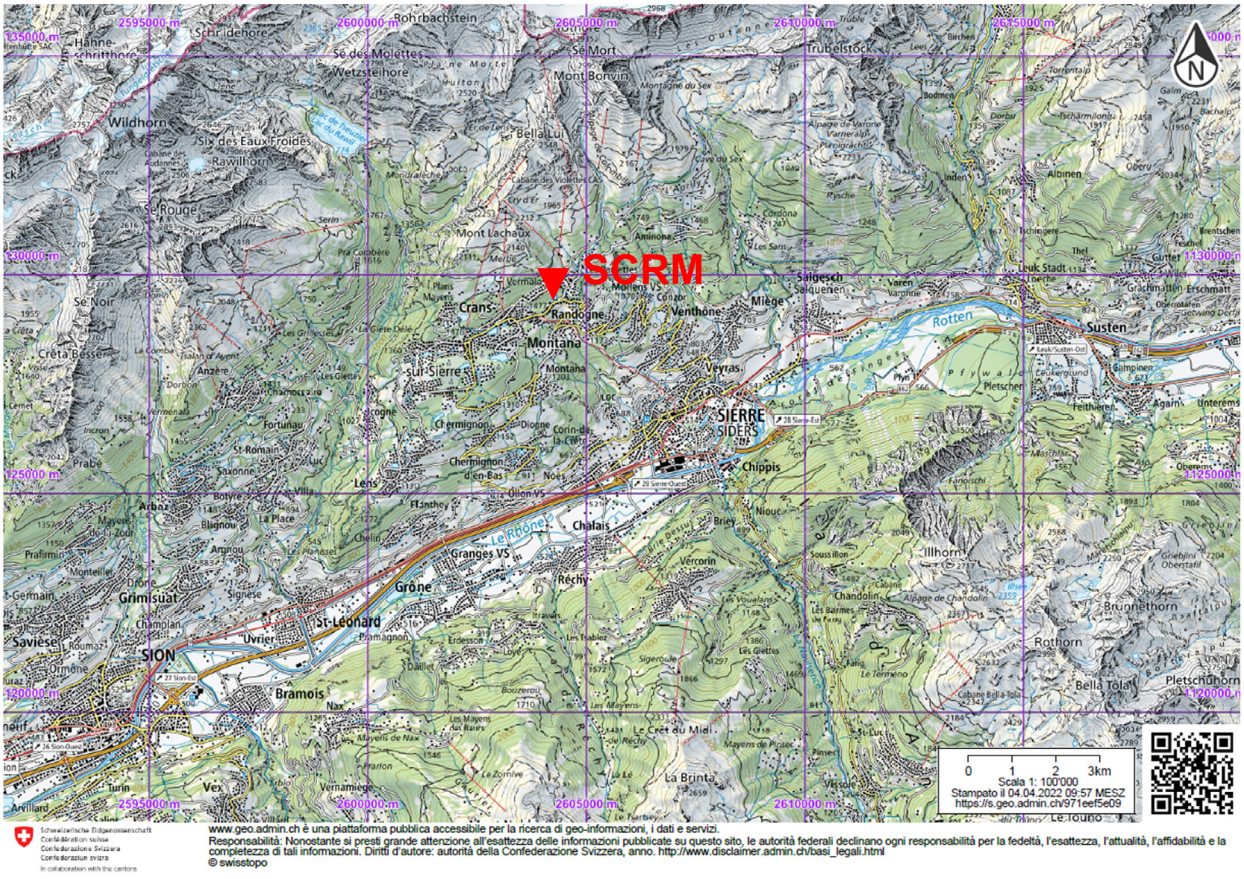

Figure 1 – Geographical location of SCRM station, on the north-western flank of the mid Swiss Rhone valley (© Swisstopo).

2. Geological setting

The site hosting SCRM is located on the steep north-western flank of the Swiss Rhône valley, overlooking Sierre/Siders. The flank is affected by mass movement of the upper weathered rock formation. The local bedrock is constituted by metasedimentary schists (marlstone, clayey schists), partially covered by moraine (till), scree or alteration silts. Specifically, station SCRM is installed at a site whose weathering layer is identified as till by the local Swiss Geological Atlas (Sheet 1287, Sierre/Siders, Swisstopo, 2018).

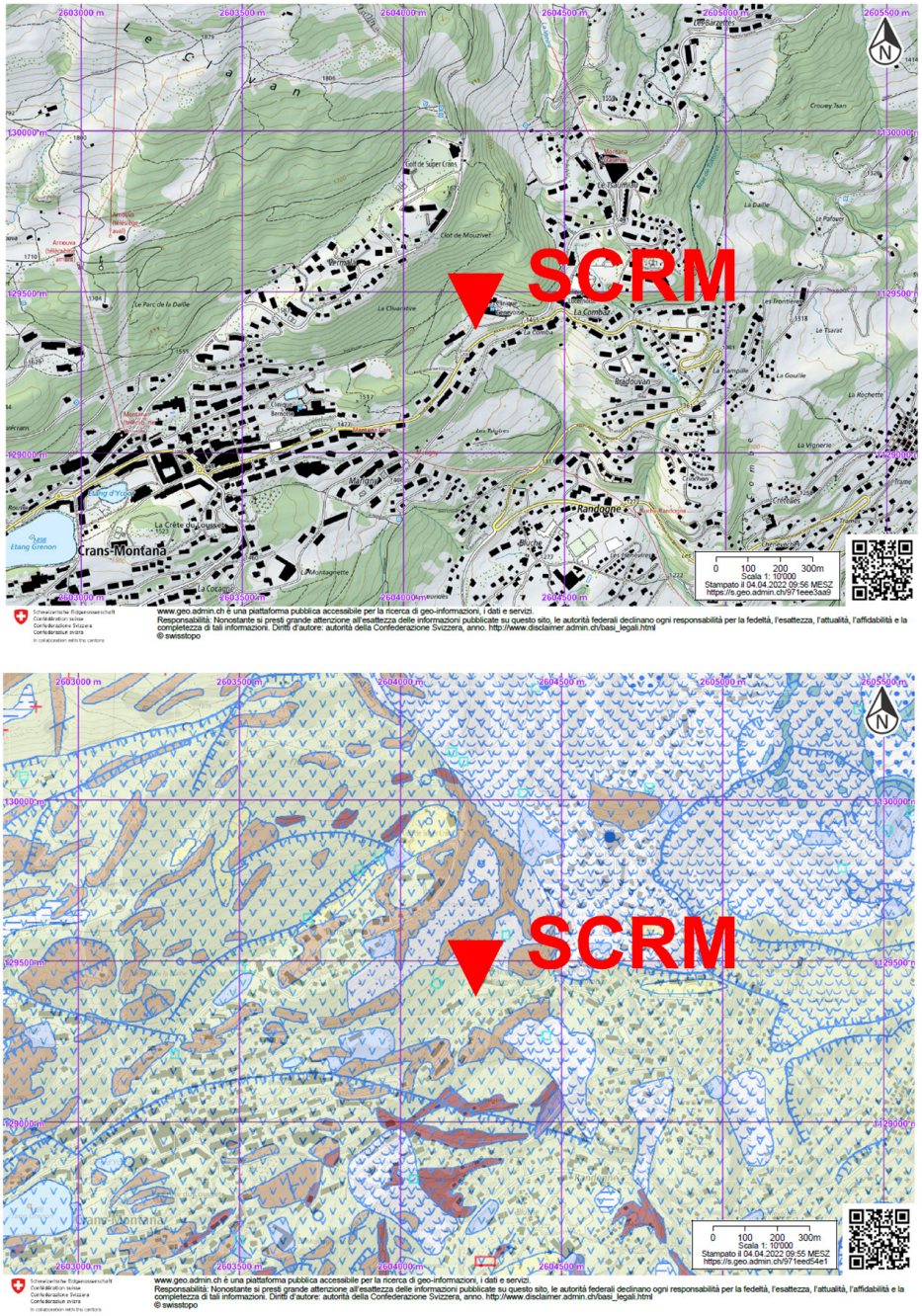

Figure 2 – Zoom on the geographical location of the SCRM station (top) and geological description of the corresponding area (bottom) according to the Swiss Geological Atlas 1:25000 (Sheet 1287, Sierre/Siders, © Swisstopo). SCRM station is located on a till formation affected by mass movement.

3. Active seismic measurements

The active seismic line was deployed few meters to south-west of station SCRM, along the side of the parking lot of the Cinique Génevoise (Figure 3).
For the sake of a comprehensive subsurface characterization, multichannel analysis of surface waves (MASW; Park et al., 1999) and P-wave refraction (Redpath, 1973) surveys were conducted.

3.1 Equipment

We used three sets of eight three-component geophones (4.5 Hz corner frequency). Each geophone set was connected to a Geode datalogger; the three Geodes were coupled for time synchronization. The seismic source was 5-kg sledgehammer, hitting a flat metal plate. The seismic source was operated at four locations (yellow stars in Figure 3).
The synchronization between the traces recorded by the geophones and the seismic source was ensured by a trigger device fastened to the hammer handle.

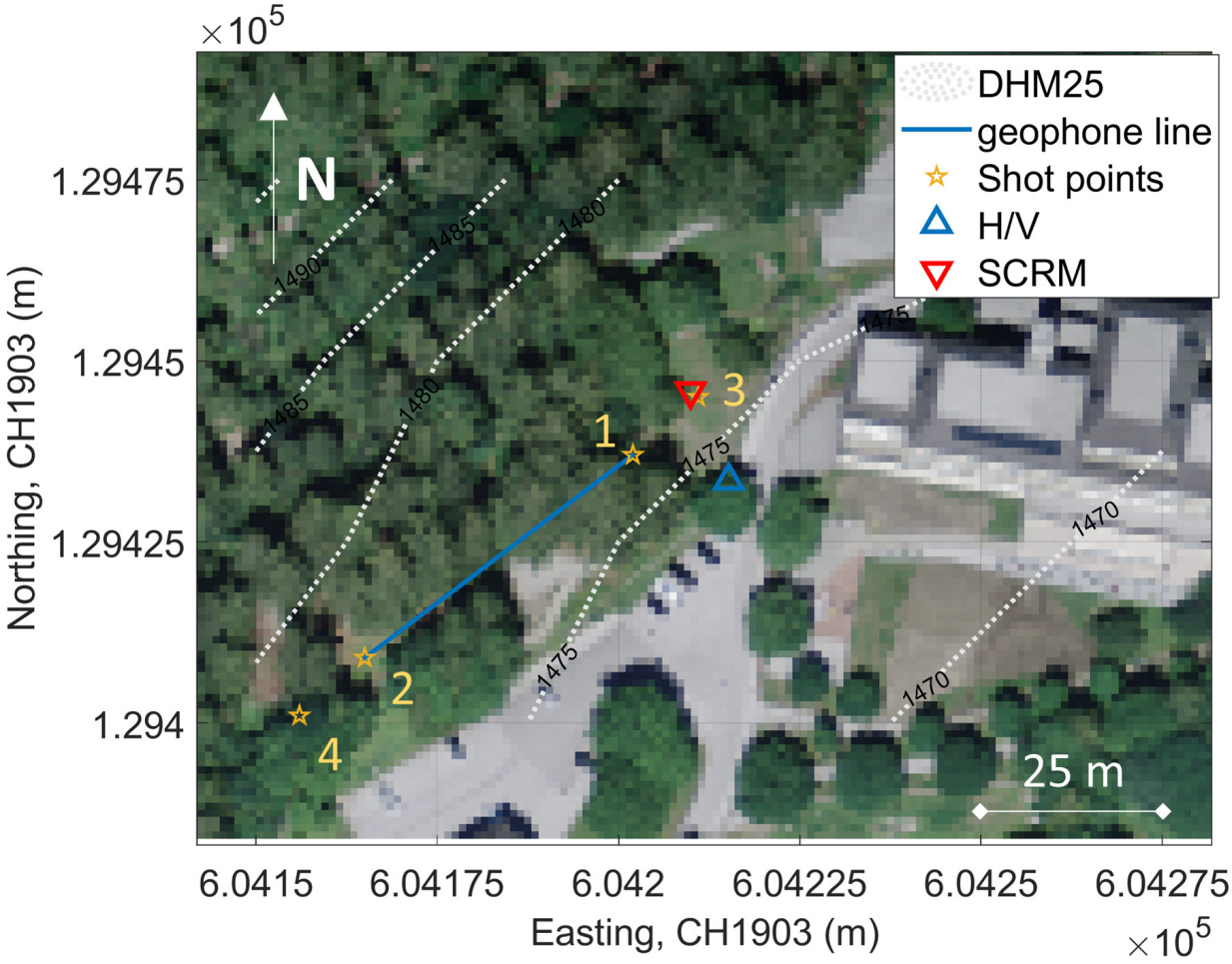

Figure 3 – Map representing the position of the targeted station (SCRM, red triangle), of the noise recording sensor (blue triangle) and of the active seismic line (blue line and yellow stars, representing the shot points: these are numbered from 1 to 4). Gray dotted lines represent the elevation lines from the DHM25 elevation model (Swisstopo, 2005), at 5 m intervals.

3.2 Geometry of the acquisition array

The seismic line was constituted by 24 3-component receivers, aligned at regular intervals of 2 m, for a total length of 46 m. The geophones were laid on the soil with metal spikes ensuring a firm coupling with the ground (Figure 4). The two horizontal components of the geophones were aligned along and perpendicularly to the seismic line (they are henceforth indicated as radial and transversal component, respectively). The array stretches from south-west to north-east, approximately perpendicular to the direction of maximum slope.

As earlier anticipated, MASW and P-wave refraction measurements were performed. As for the refraction survey, the seismic source (a sledgehammer hitting vertically a metal plate) was successively placed at the two ends of the geophone line; these shot points are henceforth referred to as shot point 1 (NE end of the array) and shot point 2 (SW end of the array). Two additional MASW shooting positions were placed externally of the array, 12 m from the two extremities of the array; these are indicated as shot point 3 (NE of the array) and shot point 4 (SW of the array, see Figure 3).

Figure 4 – Geophone array in place. The picture was taken at the north-east end of the geophone line.

3.3 Acquisition

The time-sampling parameters adopted for both MASW and refraction acquisitions were the following: sampling interval = 62.5 μs, record length = 3 s, pre-trigger delay = -0.1 s. At the seismic refraction source points, 10 hammer shots were blown; the traces generated by each blow were iteratively stacked and finally saved in a single *.sg2* file. As for the MASW acquisition, at each of the two shot points 10 hammer blows were repeated; the traces generated by each shot were separately saved in a *.sg2* file (without automatic stack). Figure 5 shows, as example of the acquisition, the vertical- and radial-component seismograms obtained from the MASW shooting with source placed to the south-west of the geophone line (shooting point 4). In Figure 6 (upper panels), the two vertical-component seismograms used for P-wave refraction analysis are displayed.

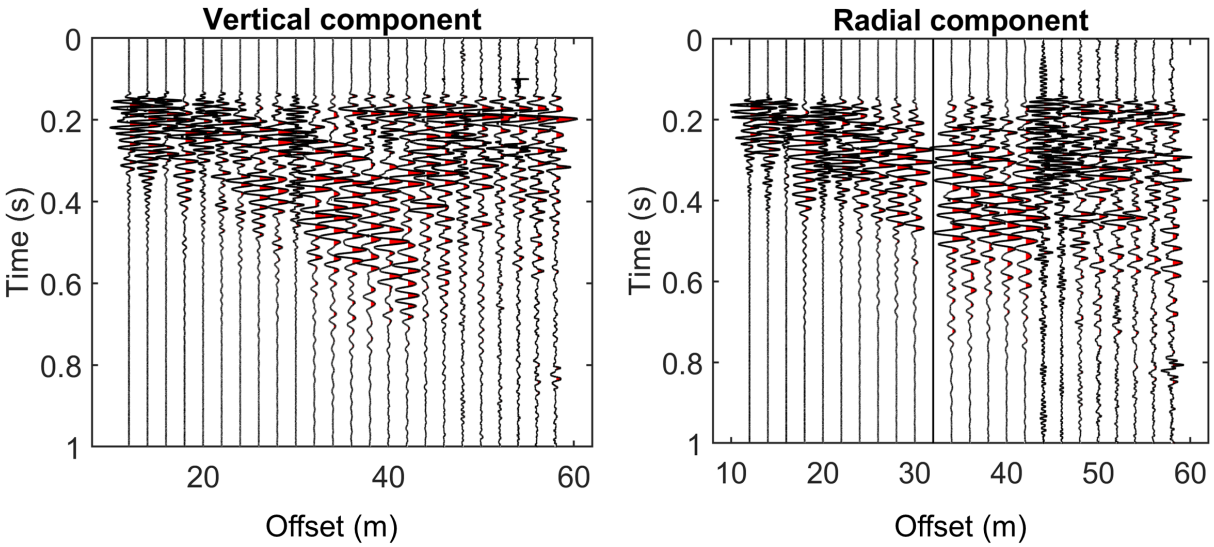

Figure 5 – Examples of seismic sections acquired for Rayleigh wave data analysis: vertical (left) and radial (right) component traces acquired with the seismic source placed 12 m to the south-west of the geophone line (shooting point 4).

3.4 Processing

3.4.1 Refraction processing

P-wave first-break arrival times were manually picked on the stacked vertical-component seismograms obtained from shooting position 1 and 2 (Figure 6, top panels). Figure 6, lower panel represents the travel-time curves, or hodocrones, obtained from each of the two positions. The two hodocrones appear to be approximately similar, thus suggesting the absence of significant lateral variations, at least in the shallow subsurface. The two travel-time curves were jointly interpreted with the intercept-time method (Reynolds, 2011); the obtained velocity profile is constituted by a shallow layer with V_P = 355 m/s and thickness = 3.2 m, overlying an intermediate layer with V_P = 2544 m/s and thickness = 4 m. The halfspace below has an estimated V_P of 3862 m/s.

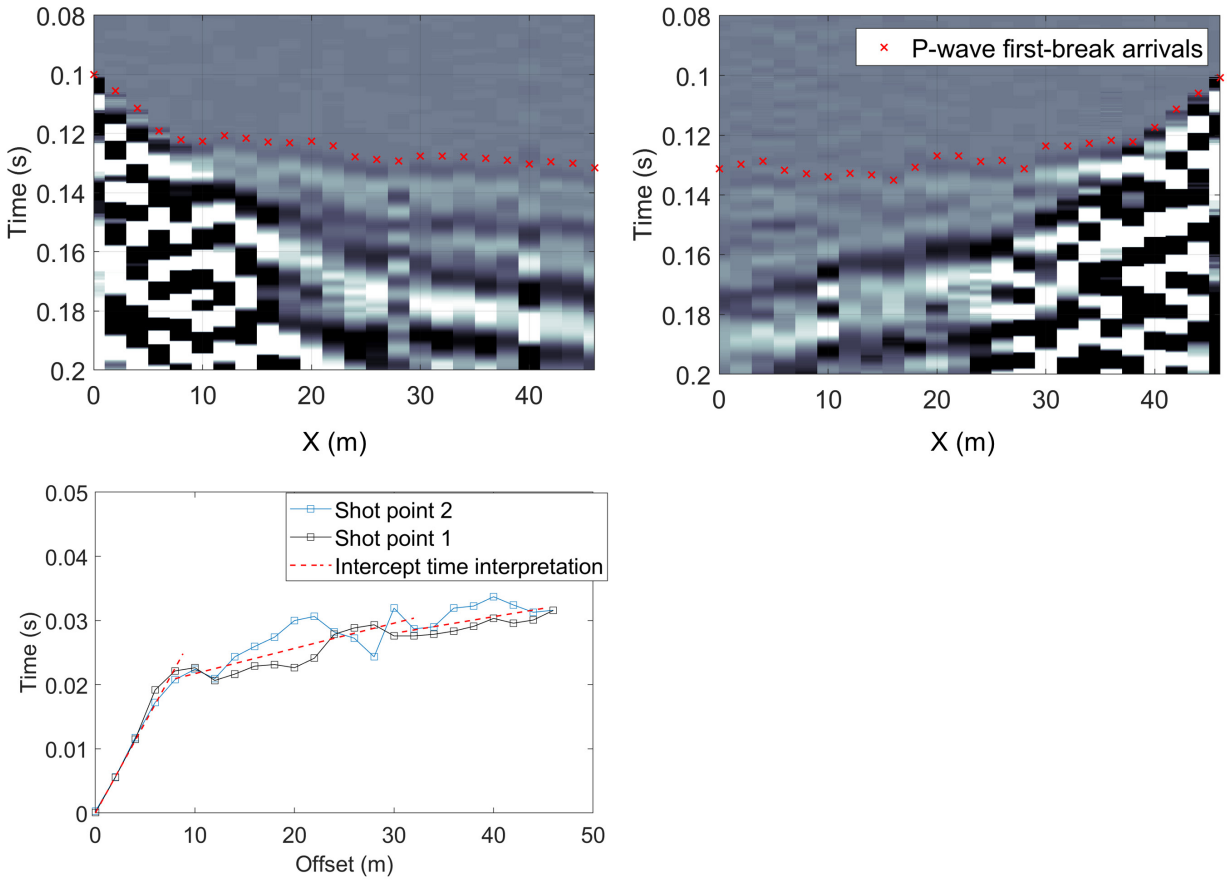

Figure 6 – P-wave refraction processing. Top panels: picked P-wave first-break arrival times from each of the two shooting positions (shot point 1, left and shot point 2, right). The X coordinate is the distance from the north-easternmost geophone. Bottom: intercept-time interpretation of the two hodocrones.

3.4.2 Rayleigh wave data f-k processing

Rayleigh wave dispersion data were extracted from the vertical and radial component seismograms of MASW acquisitions (shooting point 3 and 4). The considered seismic sections were processed by means of a 2D *f-k* (frequency – wavenumber) transform (Socco and Strobbia, 2004), in order to obtain a conversion of the recorded sets of traces from time–offset to frequency–wavenumber domain. *f-k* panels from single shot records with the same source position were summed to obtain spectral images with greater S/N ratio (O'Neill, 2003; Neducza, 2007). The energy maxima corresponding to the Rayleigh wave dispersion curves were picked on these stacked panels; spectral amplitude peaks from individual shot recordings were identified as well, and used to define the uncertainty intervals in the estimation of phase velocities (Socco et al., 2009; Boiero and Socco, 2010).
Figure 7 shows the stacked *f-k* panels from the considered seismic records (translated in the phase velocity *vs* frequency plane), as well as the corresponding picked energy maxima.

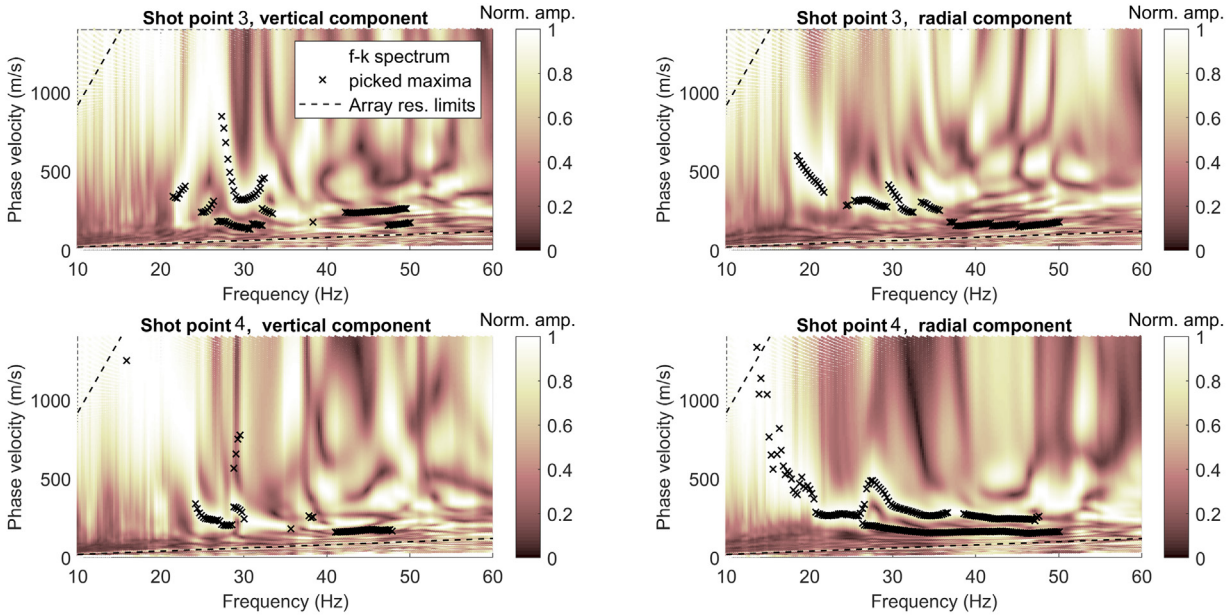

Figure 7 – Stacked normalized f-k spectra (displayed in phase velocity vs frequency) obtained from vertical and radial components of the seismic section with source positioned 12 m NE of the array (shot point 3), and 12 m from the southernmost receiver (shot point 4). Black crosses are the picked energy maxima, corresponding to Rayleigh wave dispersion curve data points; dashed back lines represent the array resolution limits.

As expected for a stiff site (Bergamo et al., 2011), the image in the *f-k* panels is not clear, with several dispersive features extending over narrow frequency bands. Nevertheless, the dispersion curves retrieved on the radial component are somewhat clearer.

The phase velocity dispersion curves from the four stacked *f-k* panels of Figure 7 are collated in Figure 8. Overall, they group into a consistent common feature. A dispersive branch spans continuously the 13 – 50 Hz frequency band, with phase velocity decreasing from ~1250 to ~160 m/s; this branch was identified as the fundamental mode of Rayleigh waves. A second branch displays a constant phase velocity of 200 m/s between 30 and 50 Hz, then a sharp increase in velocity occurs at about 28 Hz. The branch was labelled as first higher mode. Its sudden increase in phase velocity, and the small distance to the fundamental mode at 28 Hz indicate an osculation point, a feature generally associated with sharp velocity contrasts (Maraschini and Foti, 2010).

The dispersion curves from the four stacked *f-k* panels of Figure 7 were finally averaged into one curve representative for the site (red and orange lines in Figure 8); as anticipated, the uncertainty intervals are computed using the single-shot dispersion curves.

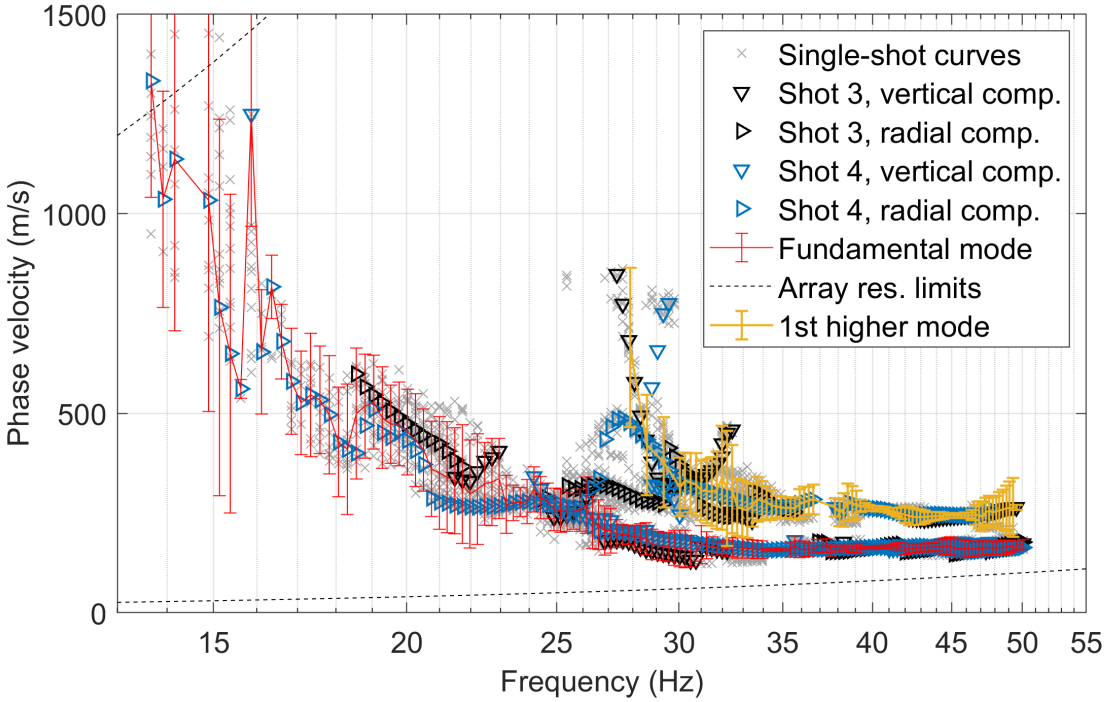

Figure 8 – Multimodal Rayleigh wave dispersion curve obtained from f-k processing. The dispersion curves from individual hammer blows (to be used for the estimation of the uncertainty intervals) are represented with gray crosses. The dispersion curves picked on the four stacked f-k panels of Figure 7 are represented with black (shooting position 3) and blue (shooting position 4) triangles; these curves were merged into a single, final curve, representative of the site (colored lines); the different colors refer to the identified modes. Black dashed lines represent the array resolution limits.

4 Ambient noise recording

4.1 Acquisition and equipment

Besides active seismic surveys, a single-station ambient noise recording measurement was performed. A Lennartz 3C 5s seismometer, connected to a Quanterra Q330 datalogger, was deployed ~10 m south of SCRM (Figure 3). The sensor was positioned on a metal tripod placed on the tarmac of the parking lot (Figure 9). The sampling frequency was 200 Hz, and the recording spanned a 1-hour time interval.

Figure 9 – Deployment of the Lennartz seismometer for microtremor recording.

4.2 Processing and interpretation

As earlier anticipated, the acquired passive traces were processed with the aim of

- estimating the H/V ratio of recorded noise, thus identifying the fundamental frequency of resonance of the site (Nakamura, 1989), thanks to the application of classical H/V methods (as implemented in Geopsy software, www.geopsy.org; classical H/V of Fäh et al., 2001, Burjanek et al., 2010).
- estimating the ellipticity of Rayleigh wave as a function of frequency, by resorting to refined algorithms (Raydec, Hobiger at al., 2009; time-frequency method, Poggi and Fäh, 2010; wavelet-based time-frequency method as implemented in Geopsy software). These methods aim at eliminating the contributions of other waves besides Rayleigh waves, to obtain a more reliable estimation of Rayleigh wave ellipticity when compared to the classical H/V technique.

The obtained results are shown in Figure 10. All the applied techniques yield consistent H/V or ellipticity curves. The common features are a broad peak at ~0.9 Hz, a sharp peak at 4.8 Hz (to be ascribed to an artificial disturbance), a third peak at ~14 Hz, and finally a continuously increasing H/V amplitude at high frequencies. The latter trend can be commonly found in H/V curves from measurements performed on sloping areas, as is the case of the current acquisition (Kleinbrod, 2018; see also Panzera et al. 2020 for similar examples).

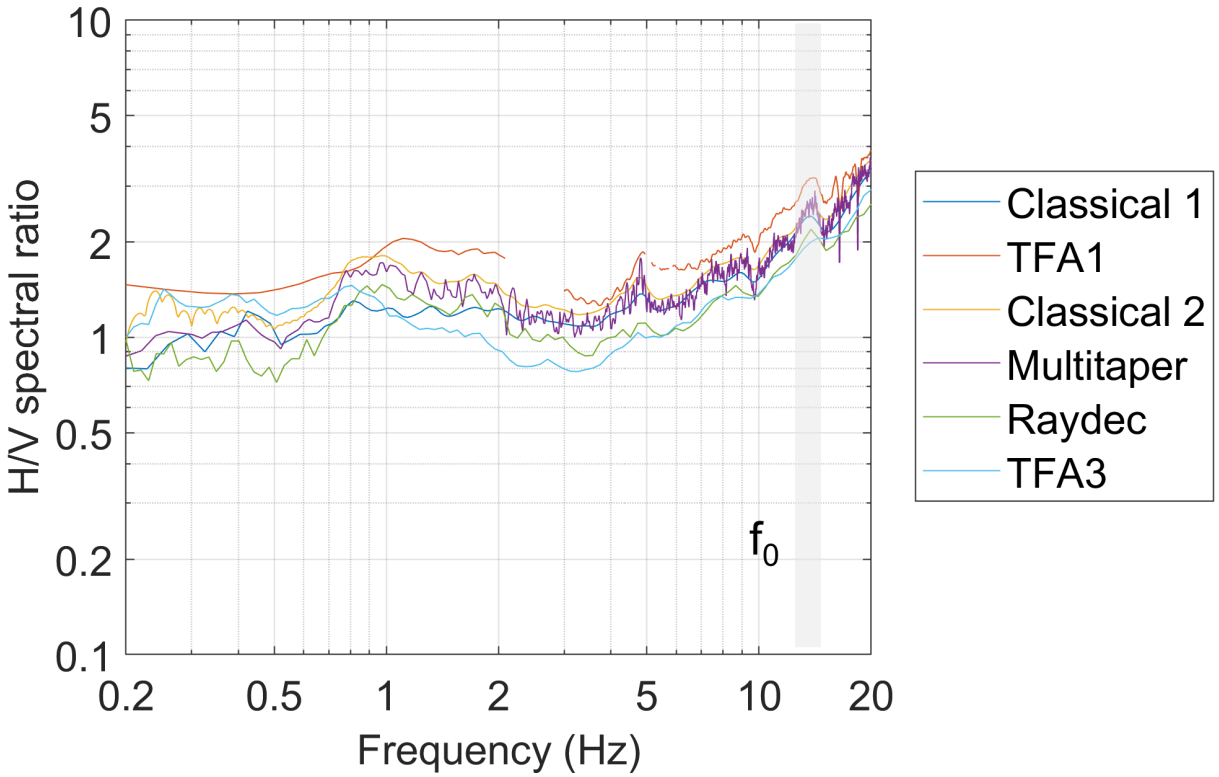

Figure 10 – H/V ratio and ellipticity curves obtained from the processing of noise recording data, using several algorithms. Classical 1: Geopsy; Classical 2: Fäh et al., 2001; TFA1: wavelet-based time-frequency method as implemented in Geopsy software; TFA3: time-frequency method, Poggi and Fäh, 2010; Raydec: Hobiger et al., 2009; multitaper: Burjanek et al., 2010. The picked fundamental frequency of resonance (f_0) is highlighted with a gray line.

To assess the origin and quality of the peaks earlier mentioned, we computed the power spectral density (PSD) of each of the three components of the ambient noise acquisition (Figure 11). From this analysis, it is possible to conclude that the peak at 4.8 Hz in the H/V curves is to be attributed to a nearby monochromatic source (possibly a pump or another artificial device), as in all three components a sharp spike is visible in the power spectral density graphs. On the other hand, the peaks at 0.9 and 14 Hz appear to be features related to the structure of the subsurface, as in their corresponding frequency bands the horizontal components do show a peak or a higher value in their PSDs, while the vertical component does not. The 0.9 Hz peak is to be ascribed to a deep impedance contrast way beyond the investigation depth of this site characterization analysis (see section 5); besides, the peak H/V amplitude is quite modest (1.2 – 1.8, Figure 10) and therefore the corresponding frequency was not identified as a one of the site resonance frequencies. Conversely, the peak at 14 Hz reaches H/V ratios between 2 – 3 (Figure 10) and possibly it is to be related to a surficial but significant velocity contrast at about 3 m depth (see section 5). Therefore, the frequency of 14 Hz was selected as the site's fundamental frequency of resonance (f_0).

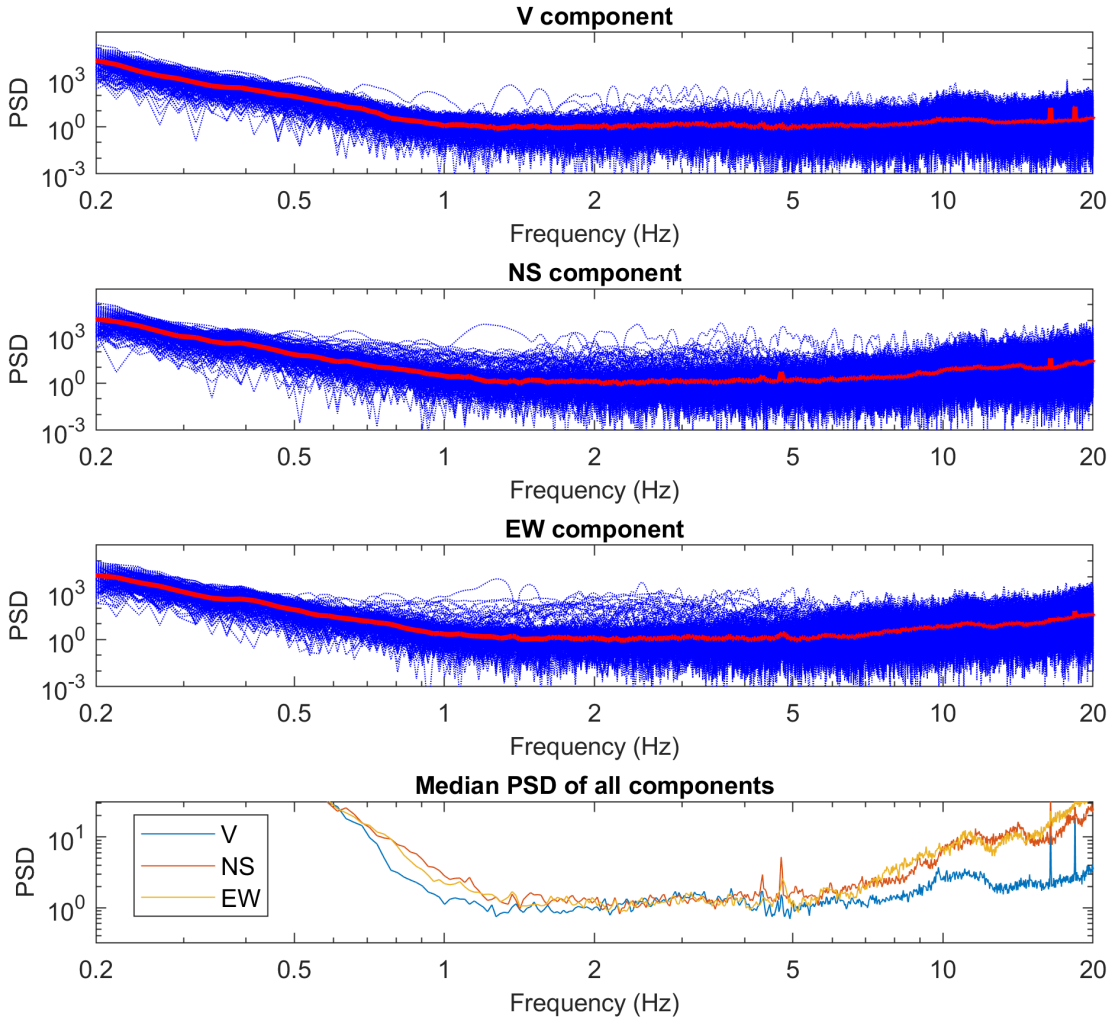

Figure 11 – Power spectral density (PSD, in arbitrary units) of the three components of the ambient noise recording: vertical (top panel), North-South (2nd panel) and East-West component (3rd panel). PSDs from 30 s signal windows are in blue, the median is represented in red. In the bottom panel the median PSDs from the three components are collated.

The ambient noise recording was also processed with the polarization tool of Burjanek et al. (2010). In Figures 12 and 13 we display the produced ellipticity (as defined in Burjanek et al., 2010, see caption of Figure 12) and strike graphs as function of frequency. The ellipticity plot (Figure 12) shows only a minor through at ~14 Hz, which corresponds to the identified f_0 peak in Figure 10. As for the polar strike (Figure 13), the 14 Hz peak does show only a modest directionality along the nort-west – south-east direction, which is approximately the downslope direction at the sensor location. A similar effect was observed in a similar setting in the site characterization analysis for the SSMNet station SHER (Hérémence, Bergamo et al. 2019). The most evident feature in the ellipticity and strike plots of Figures 12, 13 is visible at ~25 Hz; considering the high values of relative frequency of occurrence (color scale) and the narrow frequency band, it should be associated with a nearby artificial source and it is not relevant for this study.

As conclusion, we do not consider SCRM as a site with significant 2D or 3D resonance effects.

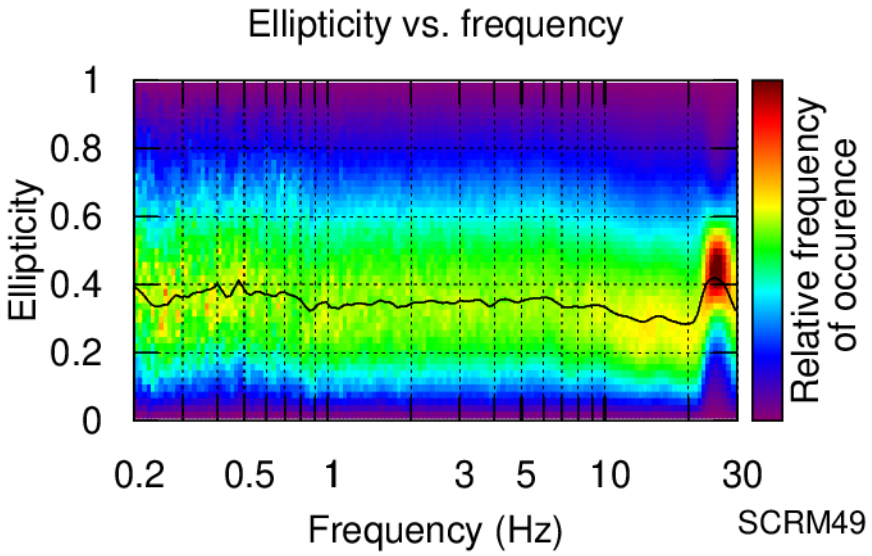

Figure 12 – Polarization analysis. Ellipticity vs frequency graph. The ellipticity is here intended as in Burjanek et al. (2010), i.e. the ratio between minor and major axes of the ellipse describing the instantaneous particle motion recorded at the soil surface.

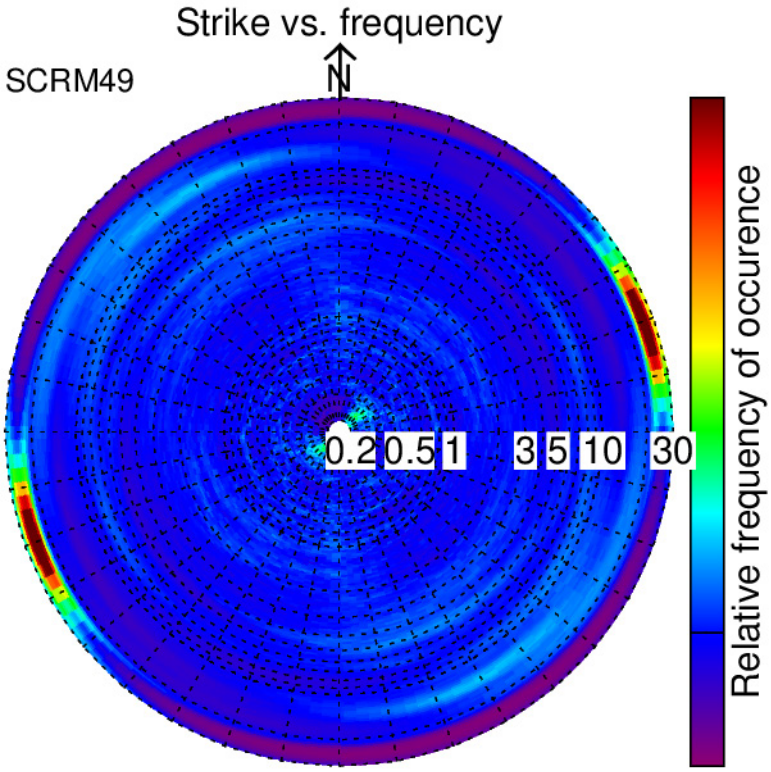

Figure 13 – Polarization analysis. Polar strike vs frequency graph.

5 Inversion of Rayleigh wave data

The Rayleigh wave dispersion curve and the ellipticity curve obtained from the processing of active and passive seismic data, respectively (see sections 3, 4) were inverted for the 1D S-wave velocity profile of the investigated site. For the inversion we used an ad-hoc code we implemented in Matlab ®. The code performs a Monte Carlo inversion, first generating a population of feasible joint V_S/V_P profiles, then computing the synthetic curves corresponding to each model, and finally evaluating the misfit with respect to the experimental data. For the solution of the forward problem we resorted to Hermann (2013).

5.1 Inversion target

In detail, the target we selected for the inversion consists of:

- The multimodal Rayleigh wave dispersion curve, as obtained from the interpretation of active surface wave data with *f-k* processing (see section 3, Figure 8). The curve spans the frequency band 13 – 50 Hz.
- To further extend the investigation depth of the inversion, we included in the inversion the Rayleigh wave ellipticity curve obtained from the single-station noise measurement processed with Raydec technique (Hobiger et al., 2009, see section 4 and Figure 10). We considered the portion of ellipticity curve between 5 and 12 Hz, which was reasonably attributed to the fundamental mode of Rayleigh wave propagation. The ellipticity estimates between 12 and 15 Hz were not included in the inversion to allow for a possible singularity at the peak (Hobiger et al., 2013); the ellipticity values > 15 Hz cannot be univocally attributed to the fundamental mode, and hence they were excluded from the inversion target.

5.2 Parameterization of the model space

For the parameterization of the subsurface model, after a number of preliminary tests, two different strategies were followed, modeling the soil column as a stack of either 6 or 5 homogeneous layers with variable thickness + halfspace. In both parameterizations, at each layer, the V_S can vary within broad Monte Carlo boundaries; the same applies to V_P, although the resulting V_S/V_P ratio must be compatible with a range of possible values of Poisson's ratios set for each layer: 0.2-0.4 for the two shallowest formations, 0.2 – 0.49 for the following intermediate layers (to allow for the possible presence of water-saturated materials), 0.2 – 0.3 for the lower halfspace. Bulk density values are attributed a priori to each layer, and they increase from 1.8 t/m^3 for the weathering formation to 2.2 t/m^3 for the halfspace. For the lower halfspaces, its S-wave velocity is forced to be larger than that of the formation above.
For each parameterization, we completed an inversion run with 10^6 randomly generated models.

5.3 Inversion results

In Figures 14 and 15, we show the results obtained from each of the two inversion runs (Figure 14: 6 layers + halfspace parameterization, Figure 15: 5 layers + halfspace parameterization). The obtained velocity profiles are similar, and so is the achieved level of match between experimental and

simulated curves (summarized by the root-mean-squared error, RMSE). The agreement between observed and synthetic curves is generally good, with the exception of the phase velocity fundamental mode at around 28 Hz, where experimental velocities are lower than the predicted ones. However, this mismatch cannot be ascribed to a particular parameterization, as both inversion runs do present the same feature; further attempts (not shown here) to fit this particular frequency band – by modifying the Monte Carlo boundaries – were not successful.

Considering the similarity among the results obtained from the two parameterizations, as final result we merge the best performing models from the two inversion run and finally select the 30 joint V_S/V_P profiles achieving the lowest RMSE.

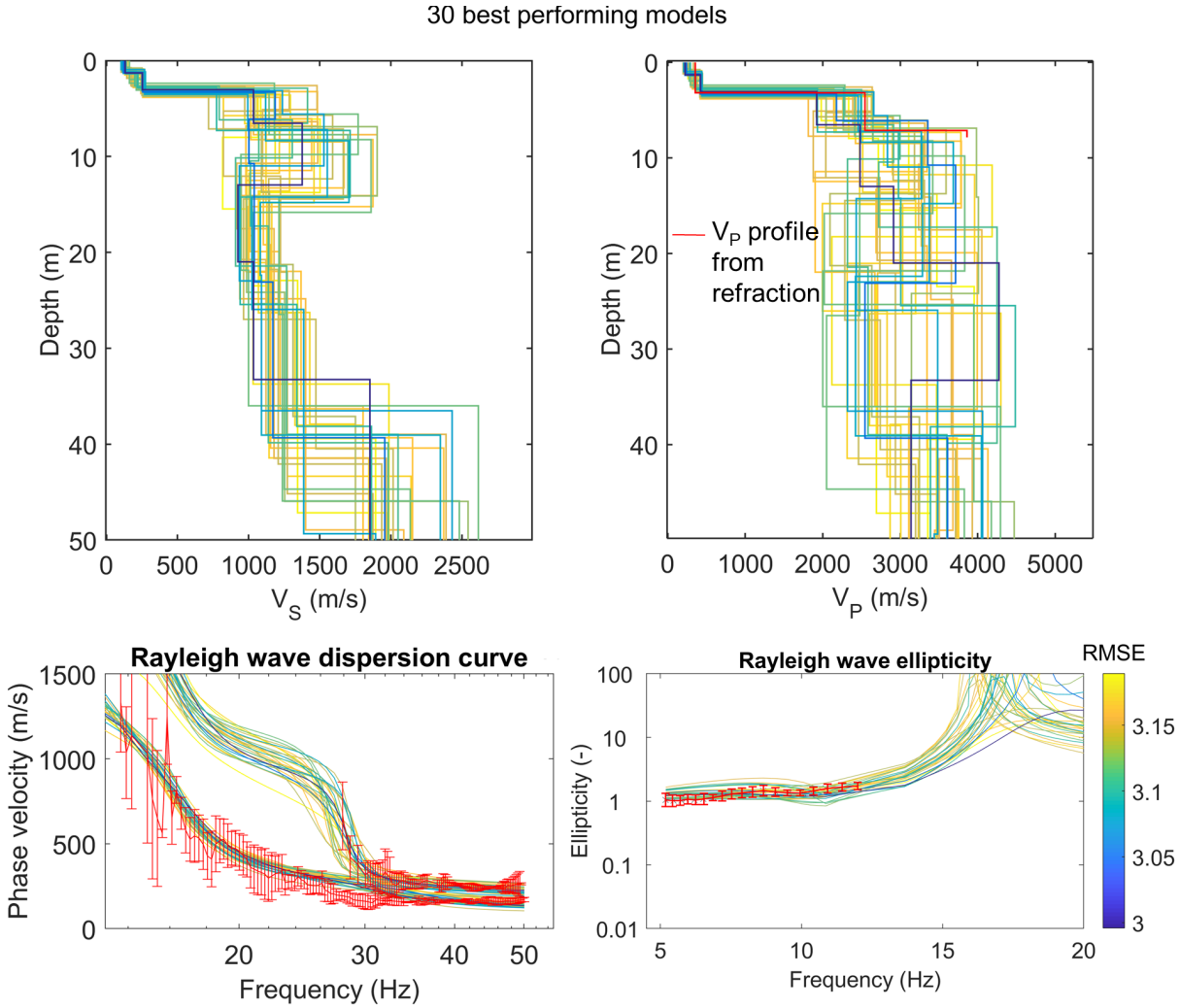

Figure 14 – 30 best performing models obtained from the 6-layer (+ halfspace) parameterization inversion run. Top: Vs and Vp profiles; bottom; fit of experimental Rayleigh wave dispersion curve (left) and ellipticity curve (right) with simulated curves.

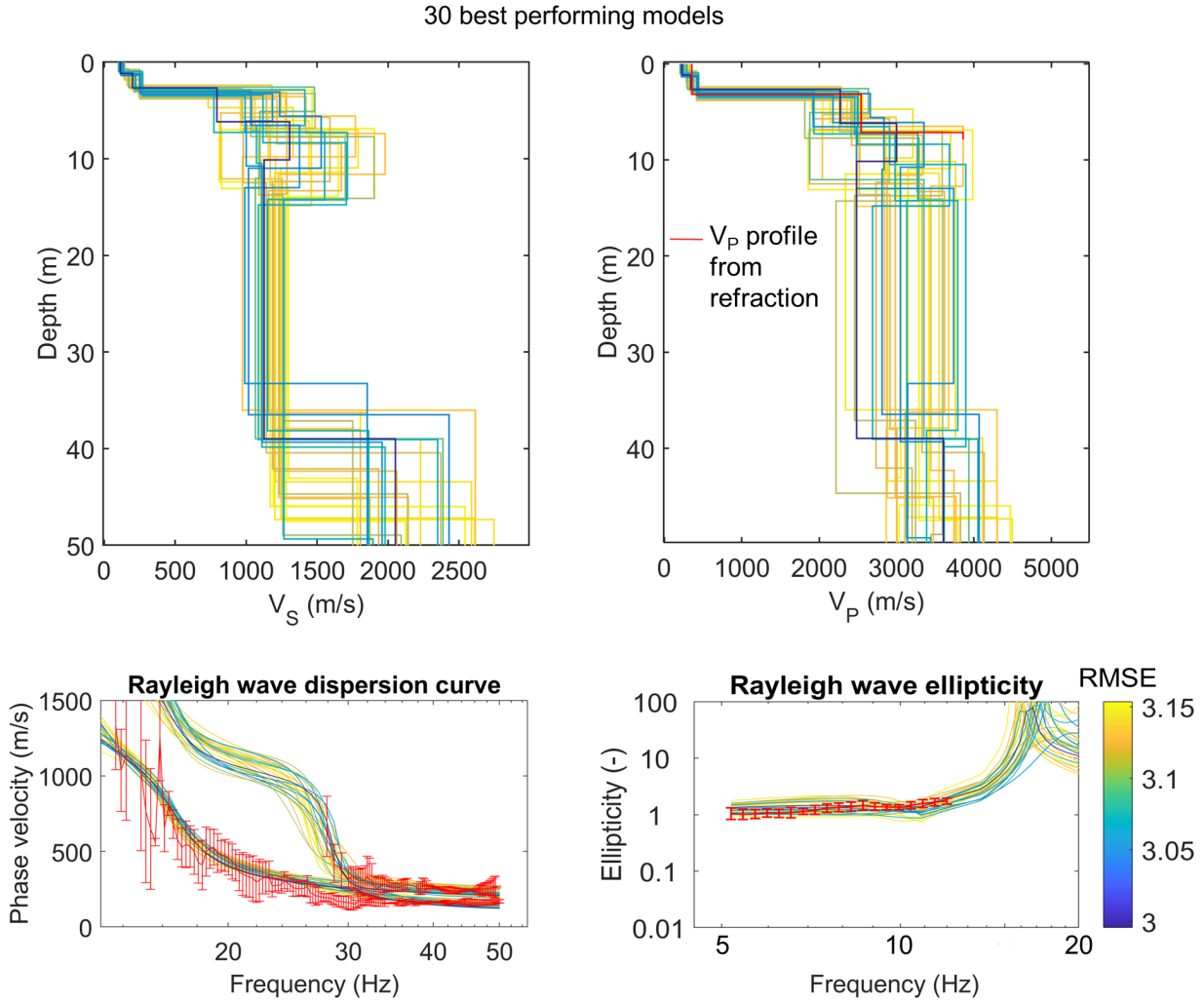

Figure 15 – 30 best performing models obtained from the 5-layer (+ halfspace) parameterization inversion run. Top: Vs and Vp profiles; bottom; fit of experimental Rayleigh wave dispersion curve (left) and ellipticity curve (right) with simulated curves.

6 Interpretation of the velocity profiles

6.1 Velocity profiles

As anticipated, the 30 velocity models from both parameterizations achieving the lowest RMSE were selected as final inversion result (Figure 16). This set of V_S/V_P velocity profiles provides a consistent description of the subsurface structure. The shallower 3.5 m present low values of V_S and V_P (~200 and 350 m/s, respectively), and they can be identified as unconsolidated surficial soil. Just below, the S-wave velocity increases abruptly to 1200 m/s (V_P to 2400 m/s). This layer, extending down to a depth of ~7 m, could be constituted by compact till, a geological formation which can have high values of stiffness (Kelly et al. 2018). The sharp velocity contrast at 3.5 m depth is to be associated with the f_0 peak in the H/V spectral ratios (Fig. 10). Between 7 and 14 m depth the S-wave velocity increments further to ~1600 m/s. This value could be attributed to a compact moraine rich in gravel, a formation found in boreholes drilled about 300 m south of SCRM site

(https://geocadast.crealp.ch/index.php?mode=display&view=carte). In another interpretation, this layer could be identified as composed by schists stiffer than those below. It should be noted that for this shallower portion of the subsurface there is a reasonable agreement between the V_P profile obtained from refraction and the P-wave velocity models obtained from the Rayleigh wave data inversion (figure 16, right panel). Between 14 and 40 m depth, the estimated S-wave velocity ranges between 1000 and 1250 m/s; this layer is probably constituted by weathered clayey/chalky schists, responsible for the mass movement observed in the area (section 2). Below, at around 40 m the V_S increases to ~2000 m/s, indicative of a stiffer rock material.

It is worth remarking that the depth range actually constrained by the Rayleigh wave dispersion curve reaches a maximum depth of 20 – 30 m. The lower depth interval 30 – 45 m is constrained by the inversion of the Rayleigh wave ellipticity curve.

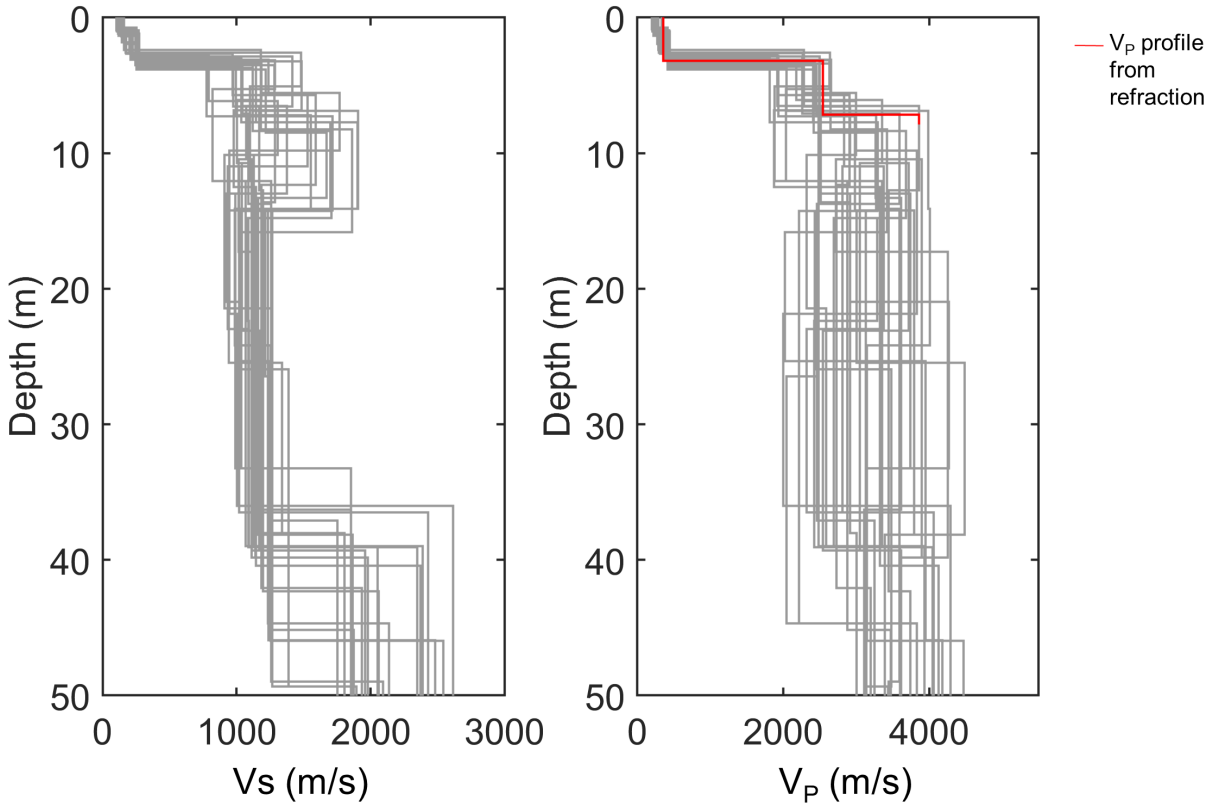

Figure 16 – Obtained V_S and V_P profiles. In the right panel, the P-wave velocity model from the interpretation of refraction data is shown.

6.2 Quarter-wavelength representation

The quarter-wavelength velocity representation (V_S^{QWL}; Joyner et al., 1981) attributes to each frequency the average velocity at a depth equal to ¼ of the corresponding wavelength. The derived quarter-wavelength impedance contrast (IC^{QWL}; Poggi et al., 2012) is the ratio between two quarter-wavelength average velocities, from the top and bottom part of the velocity profile respectively, at a given frequency; it is a powerful tool to assess the influence of resonance phenomena in soft sediment sites.

Figure 17 shows the average (over the population of the selected 30 best subsurface models) quarter-wavelength velocity (centre) and impedance contrast (bottom) representations. The obtained Vs30 (which is the average velocity corresponding to a quarter-wavelength of 30 m) is 728 m/s.
The IC^{QWL} graph shows one clear peaks at 14 Hz, to be associated with the impedance contrast at 3.5 m depth between surficial soil and moraine (Figure 16).

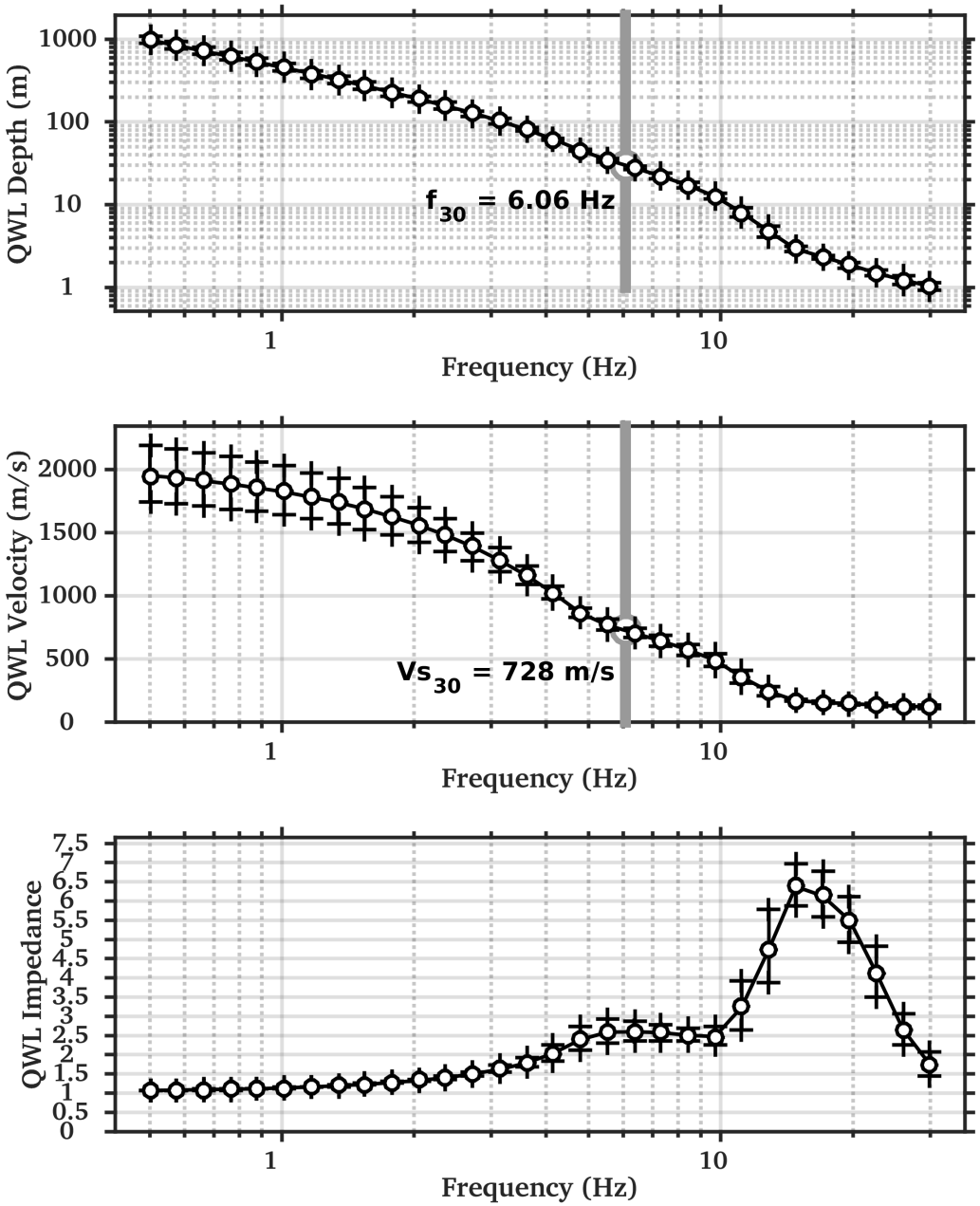

Figure 17 – Average quarter-wavelength representation of the selected velocity profiles (Figure 16). Top: depth; center: velocity; bottom: impedance contrast. The gray line in the top and center panel refers to Vs_{30}.

6.3 SH-wave transfer function

The theoretical SH-wave transfer function for vertical propagation (Roesset, 1970) was computed for the selected models (Figure 18). The transfer functions were also corrected for the Swiss reference

rock model (Poggi et al., 2011). These are compared (Figure 18) with the empirical amplification function obtained from spectral modeling (ESM; Edwards et al., 2013), relying on 28 events in the 2.5 – 7 Hz frequency band, decreasing to 10 events at lower and higher frequencies (as of 22.02.2022). The simulated SH-transfer functions are able to reproduce the main peak of the empirical amplification function at 16.5 Hz. However, simulated and empirical curves do differ in the frequency band 1.5 – 10 Hz, where synthetic amplification is around 1, while the observed one reaches values of 0.5. This discrepancy could be attributed

- To the subsurface structure below the investigation depth allowed by the retrieved Rayleigh wave data, and/or
- To the approximate method employed to refer the SH-transfer functions from the retrieved V_S profiles to the Swiss reference rock (Poggi et al. 2011). This referencing is inherently approximated as it would require an estimate of the local S-wave velocity model between the maximum investigation depth allowed by the inversion and the convergence to the Swiss reference profile.

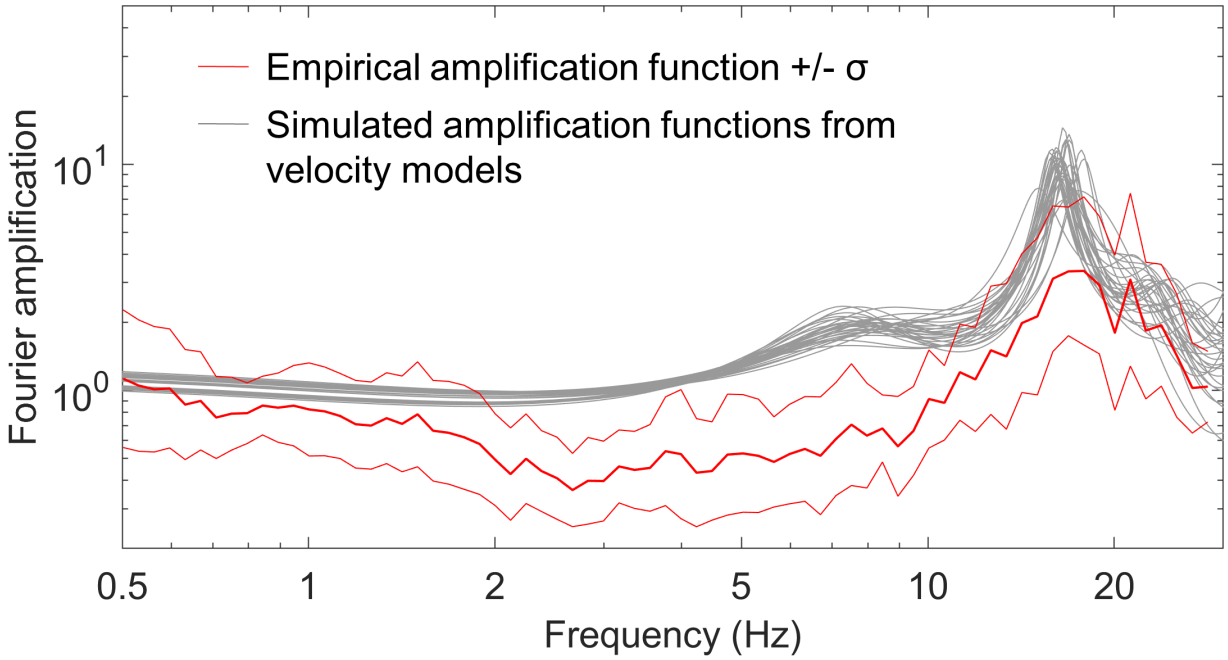

Figure 18 – Modeled SH transfer functions (gray lines) from the selected velocity profiles, corrected for the Swiss reference rock model, compared with the empirical amplification function for SCRM (red line).

7 Conclusions

Active seismic measurements and a single-station noise recording were performed to characterize the structure of the subsurface below the SSMNet station SCRM (Crans-Montana, VS). Active data were processed to derive the Rayleigh wave dispersion curve, and to identify the first-break arrivals of P-waves (later interpreted with the intercept-time method). Ambient noise data were interpreted in terms of horizontal-to-vertical (H/V) spectral ratio and also processed to estimate the ellipticity curve of

Rayleigh waves. The Rayleigh wave dispersion curve and the low-frequency portion of the ellipticity curve (5 – 11 Hz), attributed to the fundamental mode, were jointly inverted for the S-wave velocity profile at the station location.

The obtained velocity profiles present in the surficial 3.5 m low values of V_S and V_P (~200 and 350 m/s, respectively), and they can be identified as unconsolidated surficial soil. Just below, the S-wave velocity increases abruptly to 1200 m/s (V_P to 2400 m/s). This layer, extending down to a depth of ~7 m, should be constituted by compact till. Between 7 and 14 m depth the S-wave velocity increments further to ~1600 m/s. This value could be attributed to a compact moraine rich in gravel, or to a schists layer. Between 14 and 40 m depth, the estimated S-wave velocity ranges between 1000 and 1250 m/s; this layer is probably constituted by weathered clayey/chalky schists, responsible for the mass movement affecting the area. Further below, at around 40 m depth, the V_S increases to ~2000 m/s, indicative of a stiffer rock material.

The fundamental frequency (f_0) of the site, identified on the H/V_{noise} curve, is 14 Hz; it is associated with the sharp velocity contrast, at 3.5 m depth, between the surficial soil ($V_S \approx 200$ m/s) and the moraine underneath ($V_S \approx 1200$ m/s).

The estimated V_{S30} value is 728 m/s, which classifies the site as B type according to both SIA261 (SIA, 2020) and Eurocode 8 (CEN, 2004) standards. The engineering bedrock (H800, depth to shallowest layer with $V_S > 800$ m/s) is at 3.5 m depth.

References

Bergamo, P. et al., (2011). Seismic characterization of shallow bedrock sites with multimodal Monte Carlo inversion of surface wave data, Soil Dynamics and Earthquake Engineering, vol. 31 no. 3, 530-534, https://doi.org/10.1016/j.soildyn.2010.10.006.

Bergamo, P. et al., 2019. Site characterization report, station SHER (Hérémence, Route du Solitaire). Swiss Seismological Service (SED) at ETH Zurich.

Boiero, D., and L. V. Socco, 2010, Retrieving lateral variations from surface wave dispersion curves analysis: Geophysical Prospecting, **58**, 977–996

Burjanek J., G. Gassner-Stamm, V. Poggi, J.R. Moore and D. Fäh, 2010. Ambient vibration analysis of an unstable mountain slope, GJI, 180, 820-828.

CEN, 2004. Eurocode 8: Design of structures for earthquake resistance – Part 1: general rules, seismic actions and rules for buildings. European Committee for Standardization, en 1998-1 edition.

Edwards, B., Michel, C., Poggi, V., and Fäh, D., 2013. Determination of Site Amplification from Regional Seismicity: Application to the Swiss National Seismic Networks. Seismological Research Letters, 84(4).

Fäh, D., F. Kind, and D. Giardini, 2001. A theoretical investigation of average H/V ratios. GJI, 145, no. 2, 535-549.

Herrmann, R. B. (2013) Computer programs in seismology: An evolving tool for instruction and research, Seism. Res. Lettr. 84, 1081-1088, doi:10.1785/0220110096

Hobiger, M., P.-Y. Bard, C. Cornou, and N. Le Bihan, 2009. Single station determination of Rayleigh wave ellipticity by using the random decrement technique (Raydec). GRL, 36, L14303

Hobiger, M., C. Cornou, M. Wathelet, G. Di Giulio, B. Knapmeyer-Endrun, F. Renalier, P.-Y. Bard, A. Savvaidis, S. Hailemikael, Bihan N. Le, M. Ohrnberger, N. Theodoulidis, 2013. Ground structure imaging by inversions of Rayleigh wave ellipticity: sensitivity analysis and application to European strong-motion sites, Geophysical Journal International, Volume 192, Issue 1, January, 2013, Pages 207–229, https://doi.org/10.1093/gji/ggs005.

Joyner, W. B., Warrick, R. E., and Fumal, T. E. (1981). The effect of Quaternary alluvium on strong ground motion in the Coyote Lake, California, earthquake of 1979. Bulletin of the Seismological Society of America, 71(4):1333–1349.

Kelly (Harley), R. M. G., P. Bergamo, D.A. Hughes, S. Donohue, L. Barbour and K. Lynch (2018). A comparison of small strain stiffness in Till as measured by seismic refraction and barometric loading response, Quarterly Journal of Engineering Geology and Hydrogeology, 018; 51 (4): 493–502. doi: https://doi.org/10.1144/qjegh2017-040

Kleinbrod, U. (2018). Characterization of Unstable Rock Slopes Through Passive Seismic Measurements, PhD thesis, ETH Zurich.

Maraschini M., and S. Foti, 2010. A Monte Carlo multimodal inversion of surface waves. GJI, 182 (3). 1557 – 1566.

Neducza, B., 2007, Stacking of surface waves: Geophysics, 72, 51–58.

O'Neill, A., 2003, Full-waveform reflectivity for modelling, inversion and appraisal of seismic surface wave dispersion in shallow site investigations: PhD thesis, University of Western Australia, Perth, Australia.

Panzera F. et al. 2020. Site characterization report, station SENGL (Engelberg). Swiss Seismological Service (SED) at ETH Zurich.

Park, C. B., R. D. Miller, and J. Xia, 1999. Multichannel analysis of surface waves: Geophysics, **64**, 800–808.

Poggi, V., and D. Fäh, 2010. Estimating Rayleigh wave particle motion from three component array analysis of ambient vibrations. GJI, 180, no. 1, 251-267.

Poggi, V., B. Edwards and D. Fäh, 2011. Derivation of a Reference Shear-Wave Velocity model from Empirical Site Amplification. BSSA, 101, no. 1, pp. 258-274

Poggi, V., B. Edwards and D. Fäh, 2012. The quarter-wavelength average velocity: a review of some past and recent application developments. 15th WCEE, Lisbon 2012.

Redpath, B. B., 1973, Seismic refraction exploration for engineering site investigations: National Technical Information Service, Technical Report E-73-4.

Reynolds, J.M., 2011, An introduction to applied and Environmental Geophysics: John Wiley & Sons, Ltd.

Roesset, J. (1970). Fundamentals of soil amplification. In Hansen, R. J., editor, Seismic Design for Nuclear Power Plants, pages 183–244. M.I.T. Press, Cambridge, Mass.

SIA, Società svizzera degli ingengneri e degli architetti, 2020. SIA 261 - Azioni sulle strutture portanti. Società svizzera degli ingengneri e degli architetti, Zurich, Switzerland.

Socco, L.V., and C. Strobbia, 2004, Surface-wave method for near-surface characterization: a tutorial: Near Surface Geophysics, **2**, no. 4, 165-185.

Socco, L.V., D. Boiero, S. Foti, and R. Wisen, 2009, Laterally constrained inversion of ground roll from seismic reflection records: Geophysics, **74**, no. 6, G35-G45.

Swiss Federal Office of Topography, Swisstopo (2018). Atlas géologiques de la Suisse 1 :25000 : 1287, feuille de Sierre

Swiss Federal Office of Topography, Swisstopo (2005). DHM25, Das landesweite digitale Höhenmodell.